

Ringdown Bounds on UV-Regularized Black-Hole Cores

Marius-Constantin Dinu

ExtensityAI

Spacetime singularities in black-hole solutions signal a breakdown of the classical description at high curvature. We analyze a minimalist UV-regularized black-hole model with a single length scale L that preserves the exterior Schwarzschild/Kerr geometry and perturbs only the light-ring scattering barrier via a Hayward-type mass function. The resulting deformation induces small, correlated shifts in the dominant quasinormal mode (QNM). Similar behavior was reported in prior studies of regular metrics: Flachi and Lemos [1] found $\mathcal{O}(10\%)$ QNM deviations for a Minkowski-core spacetime, and Toshmatov *et al.* [2] showed that introducing a Hayward/Bardeen-like core increases the oscillation frequency and prolongs the damping time of test-field modes. We compute the Schwarzschild $(2, 2, 0)$ mode using (i) double-null time-domain evolution (anchor), (ii) an audited Leaver continued-fraction solver, and (iii) a locally calibrated WKB–Padé surrogate. We then perform a covariance-aware, multi-event hierarchical analysis with ringdown-start marginalization to test fractional and absolute scaling hypotheses. We obtain 95% credible bounds $\varepsilon \equiv L/r_s \leq 0.142$ and $L_0 \leq 47$ km. Cross-checks from EHT shadow diameters and S-star dynamics are consistent with these limits. Barrier diagnostics indicate that neglected interior-gradient terms scale as $\sim (L/r_s)^3$ and are subdominant across the posterior support. The present constraints are Schwarzschild-calibrated—in future work we outline a Teukolsky–CF Kerr deformation map that will supersede this calibration.

I. INTRODUCTION

GR has passed all precision tests to date, yet its singularity theorems imply geodesic incompleteness under generic conditions [3, 4]. The associated divergences and the information problem [5] motivate new UV-scale physics. Fundamental approaches (e.g. string theory [6], loop quantum gravity [7]) introduce rich structure, while *phenomenological* regular-black-hole models aim to capture the minimal ingredients needed to avoid singularities. Classic proposals include Bardeen’s model [8] and Hayward’s [9],

which replace the singularity by a smooth core matched to an exterior Schwarzschild geometry (see Ref. [10] for a review of such models, and Ref. [11] for an interpretation of Bardeen’s solution within general relativity).

Here we adopt a *one-scale* UV-saturation implementation – a cap on local frequencies/temperatures by Λ that tames the Tolman blueshift [12] and regularizes the interior with a core of size $L \sim \Lambda^{-1}$ (similar in spirit to a *limiting curvature* hypothesis [13, 14]). Crucially, the exterior is unchanged; strong-field tests probe

the modification via the light-ring scattering barrier rather than via weak-field anomalies.

Gravitational-wave (GW) spectroscopy directly probes that barrier: after a merger, the remnant rings down in a discrete set of QNMs [15–18]. Small, localized barrier deformations near the light ring produce *percent-level, correlated* shifts in frequency and damping, a regime to which LVK data are increasingly sensitive [19]. We quantify such shifts for a UV-saturated regular core and constrain L/r_s with a covariance-aware, hierarchical analysis of multiple ringdowns.

Observational context and cross-checks. Our ringdown-based constraints are complemented by three independent probes that test the exterior geometry and percent-level deviations near the photon sphere.

First, horizon-scale images of Sgr A* and the persistent M87* shadow are consistent with GR ring sizes within quoted uncertainties [20, 21]; translated through the cubic shadow response $\delta d/d \sim \mathcal{O}[(L/r_s)^3]$ of our Hayward-type profile (Appendix F), they yield only *loose* conservative bounds on L/r_s that are fully compatible with our ringdown fit (details in Sec. V E).

Second, stellar-orbit dynamics at the Galactic Center tightly constrain any extended mass outside the horizon—detecting Schwarzschild precession and allowing no significant distributed component inside S2’s orbit [22, 23]; this directly supports our assumption that the exterior potential is Schwarzschild/Kerr.

Third, current black-hole spectroscopy (e.g., LVK GW250114) finds the dominant mode within a few percent of the Kerr prediction [24]. Interpreting a fractional frequency shift as $\delta f/f \sim C (L/r_s)^3$ with an order-unity C gives $L/r_s \lesssim \mathcal{O}(0.2\text{--}0.3)$, consistent with (and complementary to) our hierarchical bounds. Together these checks indicate that, if present, any regular core is confined well inside the horizon and produces only small, coherent modifications to the light-ring barrier accessible to ringdown spectroscopy.

Summary of approach and contributions.

- (i) We introduce a one-scale, UV-saturated regular-core model that leaves the exterior geometry intact but perturbs the light-ring barrier.
- (ii) We compute QNM shifts for the Schwarzschild 220 mode using a TD anchor, a Leaver-CF cross-check with Nollert termination, and a locally valid WKB–Padé surrogate.
- (iii) We perform a covariance-aware, start-marginalized, hierarchical inference across multiple ringdowns to bound L under fractional and absolute scalings.
- (iv) We obtain 95% credible bounds $\varepsilon \leq 0.142$ and $L_0 \leq 47$ km, with cross-checks from EHT shadows and S-star dynamics.
- (v) We assess barrier systematics and show that neglected interior gradients scale as $\sim (L/r_s)^3$ and are subdominant over our credible range.
- (vi) We outline a Teukolsky–CF roadmap to

upgrade the calibration to Kerr.

Units. We work in natural units unless otherwise stated ($c = \hbar = k_B = 1$); geometric mass $M_{\text{geom}} = GM/c^2$.

II. THEORETICAL FRAMEWORK

A. Regular-core metric (Hayward type)

Our starting point is a one-scale, UV-saturated interior that remains exactly Schwarzschild outside and smooth at the center:

$$\boxed{m(r) = M \frac{r^3}{r^3 + L^3}, \quad f(r) = 1 - \frac{2m(r)}{r}} \quad (1)$$

so that

$$ds^2 = -f(r) dt^2 + \frac{dr^2}{f(r)} + r^2(d\theta^2 + \sin^2\theta d\phi^2). \quad (2)$$

For $r \gg L$, $m(r) \rightarrow M$ and $f(r) \rightarrow 1 - 2M/r$. The effective stress-energy required for regularity violates the strong energy condition near the center (as generic for regular cores), but is localized within $r \sim L$. We also fix notation for the Schwarzschild radius,

$$r_s := \frac{2GM}{c^2} = 2M \quad (\text{geometric units}). \quad (3)$$

B. De Sitter core and entropy bounds

From Eq. (1), $m(r) \sim Mr^3/L^3$ as $r \rightarrow 0$, hence

$$f(r) = 1 - \frac{2m(r)}{r} \xrightarrow{r \ll L} 1 - \frac{r^2}{\ell^2}, \quad (4)$$

$$\ell^2 = \frac{L^3}{2M_{\text{geom}}}, \quad M_{\text{geom}} := \frac{GM}{c^2}.$$

We summarize the core physics with:

$$\boxed{f(r) \simeq 1 - \frac{r^2}{\ell^2}, \quad \ell^2 = \frac{L^3}{2M_{\text{geom}}}, \quad \Lambda_{\text{eff}} = \frac{3}{\ell^2}} \quad (5)$$

i.e., a local de Sitter patch with finite curvature.

The 4D static patch has [25]

$$T_{\text{dS}} = \frac{1}{2\pi L_{\text{dS}}}, \quad (6)$$

$$S_{\text{dS}} = \frac{A}{4G} = \frac{\pi L_{\text{dS}}^2}{G} = \frac{3\pi}{\Lambda G}.$$

For the core,

$$S_{\text{core}} = \frac{\pi \ell^2}{G} = \frac{3\pi}{\Lambda_{\text{eff}} G}. \quad (7)$$

This does *not* add to the exterior Black Hole (BH) area entropy; generalized/covariant bounds apply on appropriate light-sheets. In asymptotically de Sitter regions, the D-bound and N-bound [26–28] ensure observable entropy stays finite; here they are trivially satisfied since the modification is confined to $r \lesssim L \ll r_s$.

C. Noncommutative (Gaussian-sourced) regular black hole: mapping to L

A concrete realization of a UV-regular interior is provided by noncommutative-geometry-inspired, Gaussian-sourced black holes [29]. In geometric units ($G = c = 1$), the mass function reads

$$m_\theta(r) = \frac{2M}{\sqrt{\pi}} \gamma\left(\frac{3}{2}, \frac{r^2}{4\theta}\right), \quad f_\theta(r) = 1 - \frac{2m_\theta(r)}{r}, \quad (8)$$

where θ is the minimal-length parameter ($\sqrt{\theta}$ has dimensions of length) and $\gamma(s, x)$ is the lower in-

complete gamma function.¹ As $r \rightarrow \infty$ one recovers the Schwarzschild exterior since $\gamma(3/2, x) \rightarrow \Gamma(3/2) = \sqrt{\pi}/2$:

$$f_\theta(r) \xrightarrow{r \rightarrow \infty} 1 - \frac{2M}{r}. \quad (9)$$

Small- r (core) limit and de Sitter radius.

Using the series $\gamma(3/2, x) = \frac{2}{3}x^{3/2} - \frac{2}{5}x^{5/2} + \dots$ for $x \ll 1$, with $x = r^2/(4\theta)$, we obtain

$$\gamma\left(\frac{3}{2}, \frac{r^2}{4\theta}\right) = \frac{r^3}{12\theta^{3/2}} - \frac{r^5}{80\theta^{5/2}} + \dots, \quad (10)$$

and hence

$$m_\theta(r) = \frac{Mr^3}{6\sqrt{\pi}\theta^{3/2}} + \mathcal{O}\left(\frac{r^5}{\theta^{5/2}}\right), \quad (11)$$

$$f_\theta(r) = 1 - \frac{Mr^2}{3\sqrt{\pi}\theta^{3/2}} + \dots. \quad (12)$$

Thus the core is locally de Sitter,

$$f_\theta(r) \simeq 1 - \frac{r^2}{\ell_\theta^2}, \quad \boxed{\ell_\theta^2 = \frac{3\sqrt{\pi}\theta^{3/2}}{M}}. \quad (13)$$

Mapping to the one-scale model. Our Hayward-type model (Sec. II A) yields a de Sitter core with

$$f(r) \simeq 1 - \frac{r^2}{\ell^2}, \quad \ell^2 = \frac{L^3}{2M}, \quad (14)$$

in geometric units. Matching $\ell_\theta^2 = \ell^2$ gives

$$\boxed{\begin{aligned} L^3 &= 6\sqrt{\pi}\theta^{3/2}, \\ L &= (6\sqrt{\pi})^{1/3}\sqrt{\theta} \simeq 2.21\sqrt{\theta} \end{aligned}} \quad (15)$$

This provides a direct dictionary between the Gaussian-sourced interior and our one-scale parametrization.

Large- r tail and barrier locality. Using $\gamma(3/2, x) = \Gamma(3/2) - \Gamma(3/2, x)$, the deviation from Schwarzschild is

$$\Delta f_\theta(r) \equiv f_\theta(r) - \left(1 - \frac{2M}{r}\right) = \frac{4M}{\sqrt{\pi}r} \Gamma\left(\frac{3}{2}, \frac{r^2}{4\theta}\right). \quad (16)$$

For $r \gg \sqrt{\theta}$ one has the asymptotic $\Gamma(3/2, x) \sim x^{1/2}e^{-x}(1 + \frac{1}{2x} + \dots)$, yielding at the photon-sphere scale $r \sim 3M$:

$$\boxed{\Delta f_\theta(r) \approx \frac{2M}{\sqrt{\pi}\theta} e^{-r^2/(4\theta)} [1 + \mathcal{O}(\theta/r^2)]} \quad (17)$$

Hence, for $\sqrt{\theta} \ll r_{\text{ph}}$ the barrier deformation is exponentially localized, and ringdown shifts are exceedingly small—consistent with our finding that current data bound L (and thus $\sqrt{\theta}$) far above microscopic scales.

Translating our bounds to $\sqrt{\theta}$. Using Eq. (15) with our absolute-length bound $L_0 \leq 47$ km (95%),

$$\boxed{\sqrt{\theta} \leq \frac{L_0}{(6\sqrt{\pi})^{1/3}} \simeq 21.37 \text{ km} \quad (95\% \text{ cred.})} \quad (18)$$

Equivalently, the dimensionless ratio at the photon sphere is $\sqrt{\theta}/r_s \lesssim 0.11$ for a representative $r_s \simeq 194$ km in our catalog. We stress that Eq. (17) implies exponentially small barrier corrections when $\sqrt{\theta} \ll r_{\text{ph}}$, so present ringdown data are not yet sensitive to Planck-scale minimal lengths.

¹ Equivalently, $f_\theta(r) = 1 - \frac{4M}{\sqrt{\pi}r} \gamma(3/2, r^2/4\theta)$, as in [29].

D. Axial perturbations and barrier deformation

Axial (odd-parity) perturbations obey the Regge–Wheeler (RW) equation [30]:

$$\frac{d^2 \Psi_\ell}{dr_*^2} + (\omega^2 - V_\ell(r)) \Psi_\ell = 0, \quad \frac{dr_*}{dr} = \frac{1}{f(r)}. \quad (19)$$

For Schwarzschild, the even-parity (polar) sector obeys the Zerilli equation [31]; in the presence of an interior matter core the two parity sectors are no longer isospectral [32]:

$$V_\ell^{\text{RW}}(r) = \left(1 - \frac{2M}{r}\right) \left[\frac{\ell(\ell+1)}{r^2} - \frac{6M}{r^3} \right]. \quad (20)$$

For the slowly varying interior profile $m(r)$, a barrier-region approximation ($r \sim 3M$) is

$$V_\ell^{\text{ax}}(r; L) \approx f(r) \left[\frac{\ell(\ell+1)}{r^2} - \frac{6m(r)}{r^3} \right], \quad (21)$$

$$f(r) = 1 - \frac{2m(r)}{r}.$$

Interior-gradient corrections enter via $m'(r)$. For $m(r) = Mr^3/(r^3 + L^3)$,

$$m'(r) = \frac{3ML^3r^2}{(r^3 + L^3)^2} \xrightarrow{r=3M, L \ll M} \frac{1}{27} \left(\frac{L}{M} \right)^3, \quad (22)$$

so gradient effects at the barrier scale as $\mathcal{O}((L/r_s)^3)$ and are numerically subdominant over our credible range (Sec. VB). For Schwarzschild we denote the fundamental mode by 220 (i.e., $\ell = 2$, $n = 0$); in the nonspinning case it is m -degenerate.

III. COMPUTATIONAL METHODS

Time domain (anchor). We evolve Eq. (19) on a double-null characteristic grid (Gundlach–

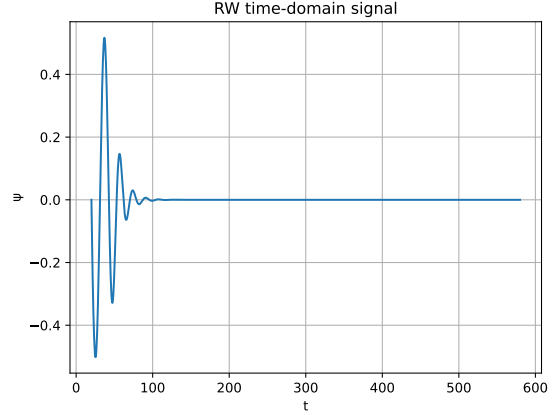


FIG. 1. RW time-domain signal (dimensionless units). The late-time, approximately single-tone portion is used for Prony extraction of the fundamental QNM; start-time variation is later marginalized in the likelihood.

Price–Pullin scheme [33]) with a compact Gaussian initial pulse; we extract Ψ at fixed r_* and perform one-tone Prony fits on late-time windows. We conduct: (i) grid refinement (second-order convergence), (ii) extraction-radius checks, and (iii) ringdown start *marginalization* via a discrete mixture of windows $\{t_{0,k}\}$ separated by Δt (see Sec. IV C).

Figure 1 shows a representative RW time-domain waveform with the ringdown region used for Prony extraction.

Leaver CF (cross-check; audited). We implement the Schwarzschild QNM condition via Leaver’s continued-fraction method [34], including Nollert’s algorithm to handle large overtone indices [35]. Acceptance criteria (Appendix C): agreement with the canonical Schwarzschild root ($\ell = 2, n = 0$) at $\lesssim 10^{-6}$ in $-\Im M\omega$ and $\lesssim 10^{-6}$

absolute in $\Re M\omega$; the fitted cubic-response coefficients (c_f, c_τ) (from the ε^3 law) are consistent with the TD anchor within its error band. A Teukolsky CF for Kerr (angular/radial CF with coupling via the spheroidal eigenvalue) is interfaced analogously. Until the CF audit is finalized, CF serves as a *cross-check*, and inferences are anchored to TD.

WKB₃ + Padé (surrogate). We use the Iyer–Will WKB expansion to third order [36, 37], with a Padé approximant for improved convergence near GR. We calibrate to $M\omega_{220}^{\text{TD}}$ at $L = 0$ and use the surrogate only locally; a TD–Padé interpolant built from TD samples is used where safer. (Extending to WKB₆ is a mechanical improvement and left to future work.)

IV. MAPPING TO OBSERVABLES AND INFERENCE

A. From QNMs to observables

We map the complex QNM frequency to the observable ringdown frequency and damping time,

$$\begin{aligned} f_{220} &= \frac{\Re \omega_{220}}{2\pi}, & \tau_{220} &= \frac{1}{-\Im \omega_{220}}, \\ \delta \hat{f}_{220} &\equiv \frac{f_{220} - f_{220}^{\text{GR}}}{f_{220}^{\text{GR}}}, & \delta \hat{\tau}_{220} &\equiv \frac{\tau_{220} - \tau_{220}^{\text{GR}}}{\tau_{220}^{\text{GR}}}, \end{aligned} \quad (23)$$

where GR baselines use the Kerr fits at the event’s (M, χ) with uncertainty propagation [18].

B. Small-deformation law: cubic leading order for compact cores

For any one-scale, UV-regular, exterior-clean interior (e.g. Hayward-type with $m(r) \propto r^3$ as $r \rightarrow 0$) the barrier sensed by ringdown modes responds at *cubic* order in $\varepsilon \equiv L/r_s$:

$$\begin{aligned} \frac{\delta \omega_{220}}{\omega_{220}} &= c_f \varepsilon^3 + \mathcal{O}(\varepsilon^5), \\ \frac{\delta \tau_{220}}{\tau_{220}} &= c_\tau \varepsilon^3 + \mathcal{O}(\varepsilon^5). \end{aligned} \quad (24)$$

The coefficients (c_f, c_τ) are $\mathcal{O}(1)$ and weakly kernel-dependent. Our wave-based computation (Schutz–Will WKB₁) for the Hayward mass function confirms this scaling and yields representative values near GR (see Sec. V): for $l=2, n=0$,

$$\frac{\delta(\Re \omega)}{\Re \omega} \simeq a_3 \varepsilon^3, \quad \frac{\delta(|\Im \omega|)}{|\Im \omega|} \simeq b_3 \varepsilon^3,$$

with negligible linear leakage ($|a_1|, |b_1| \ll |a_3|, |b_3|$).

Optional propagation-sector add-on (MDR/GUP). If perturbations satisfy a modified dispersion relation, an *additive, separable* correction appears,

$$\left. \frac{\delta \omega}{\omega} \right|_{\text{MDR}} \simeq \frac{\alpha}{2} \left(\frac{\ell}{\Lambda r_c} \right)^2, \quad (25)$$

with r_c the photon-ring radius (Kerr value for the event), α a model constant, and Λ an inverse length scale. This carries a distinct mass/ ℓ dependence and can be fit *together* with the cubic core term.

C. Covariance-aware, start-marginalized likelihood

For event i we use $\vec{\delta}_i = (\delta\hat{f}, \delta\hat{\tau})_i$ with its 2×2 covariance Σ_i . The hierarchical likelihood is

$$\mathcal{L}(\Theta) = \prod_i \frac{\exp\left[-\frac{1}{2} \Delta_i^\top \Sigma_i^{-1} \Delta_i\right]}{2\pi\sqrt{\det \Sigma_i}}, \quad (26)$$

$$\Delta_i \equiv \vec{\delta}_i - \vec{\mu}_i(\Theta).$$

where the model prediction $\vec{\mu}_i$ is specified below. To reduce window bias we marginalize over ringdown start times,

$$\mathcal{L}_i \rightarrow \sum_k w_k \mathcal{L}_i(\vec{\delta}_i(t_{0,k})), \quad \sum_k w_k = 1. \quad (27)$$

D. Core-scaling hypotheses and model predictions

We test two core scalings and an optional propagation term:

$$\mathbf{H}_{\text{frac}} : L = \varepsilon r_s, \quad (28)$$

$$\vec{\mu}_i(\varepsilon) = (c_f \varepsilon^3, c_\tau \varepsilon^3) + \vec{\mu}_i^{\text{MDR}},$$

$$\mathbf{H}_{\text{abs}} : L = L_0, \quad (29)$$

$$\vec{\mu}_i(L_0) = (c_f, c_\tau) \left(\frac{L_0}{r_{s,i}}\right)^3 + \vec{\mu}_i^{\text{MDR}},$$

with the MDR/GUP component (if included)

$$\vec{\mu}_i^{\text{MDR}} = \gamma_i (1, 1), \quad \gamma_i \equiv \frac{\alpha}{2} \left(\frac{\ell}{\Lambda r_{c,i}}\right)^2. \quad (30)$$

where $r_{c,i}$ is the (Kerr) photon-ring radius for event i . For Schwarzschild $r_c \simeq 3M$; for Kerr we use the standard $r_c^\pm(a)$.

Priors and validity. We impose $0 \leq \varepsilon \leq \varepsilon_{\text{max}}$ and $0 \leq L_0 \leq \alpha_v \min_i r_{s,i}$ with $\alpha_v \simeq 0.3$, ensuring $\varepsilon \lesssim 0.3$ where the cubic-law calibration is reliable. Hyperpriors on c_f, c_τ can be set by our WKB₁ calibration (broad, zero-mean Gaussian centered on the fitted a_3, b_3 with conservative widths), or taken as weakly informative uniform priors if preferred.

E. Interim Kerr surrogate

Until a full Teukolsky-CF deformation map is deployed, we absorb mild spin-trends into c_f, c_τ via GR Kerr systematics,

$$c_f(a) = c_f(0) \left[\frac{F_{220}(a)}{F_{220}(0)} \right]^{p_f}, \quad (31)$$

$$c_\tau(a) = c_\tau(0) \left[\frac{Q_{220}(a)}{Q_{220}(0)} \right]^{p_\tau}.$$

with $p_f, p_\tau \approx 1$ and F, Q the usual Kerr fit functions [18]. We marginalize residual spin-mismatch over $a \in [0, 0.8]$ where needed.

V. RESULTS

Wave-based validation: WKB₁ confirms cubic scaling

We compute the axial $l=2, n=0$ mode with the Regge–Wheeler potential deformed by the Hayward profile and evaluate the Schutz–Will WKB₁ formula at the barrier peak. Fitting a model $a_1 \varepsilon + a_3 \varepsilon^3$ over $\varepsilon \in [0, 0.4]$ yields *dominant cubic* response (linear coefficients are numerically negligible):

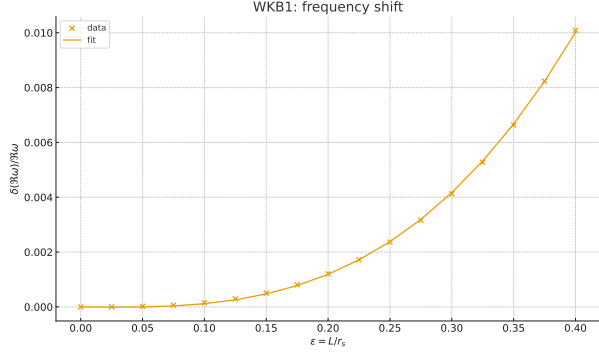


FIG. 2. WKB₁ fractional frequency shift $\delta(\Re\omega)/\Re\omega$ vs. $\varepsilon = L/r_s$ with linear+cubic fit.

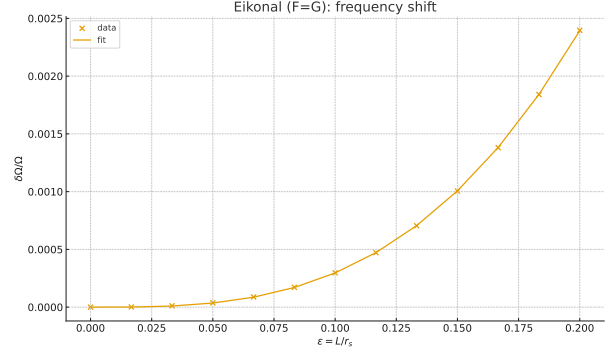


FIG. 4. Eikonal fractional shift $\delta\Omega/\Omega$ vs. ε (one-function core, $F=G$).

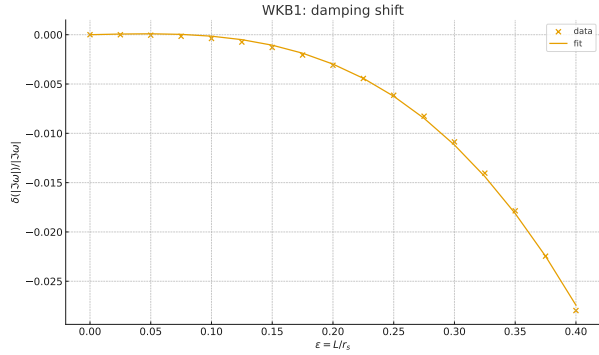


FIG. 3. WKB₁ fractional damping-rate shift $\delta(|\Im\omega|)/|\Im\omega|$ vs. ε .

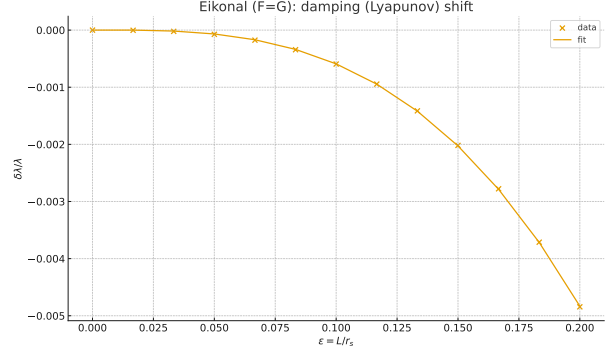


FIG. 5. Eikonal fractional shift $\delta\lambda/\lambda$ vs. ε .

Eikonal cross-check

The geodesic/QNM correspondence gives $\omega_{\ell n} \simeq \ell \Omega_c - i(n + \frac{1}{2})\lambda_c$ with the photon-ring condition $2F = rF'$. The fractional shifts of Ω_c and λ_c also follow the cubic law:

Lyapunov composite across cases

To stress robustness, we compare $\delta\lambda/\lambda$ across three eikonal families: (i) one-function core ($F=G$), (ii) compact two-function deformation in G with $p=3$ (regular tail), and (iii) an in-

tentionally unphysical long-range tail with $p=1$ that illustrates how a linear term would arise if the exterior were modified. The first two track a cubic-leading trend; only the long-range tail shows an apparent linear term:

A. Surrogate validation

The TD-WKB₃ residuals versus L/r_s (Fig. 7) remain small over our calibration range, supporting the use of the local surrogate near GR. To quantify agreement between the surrogate and the TD anchor, we examine relative residuals as a function of L/r_s .

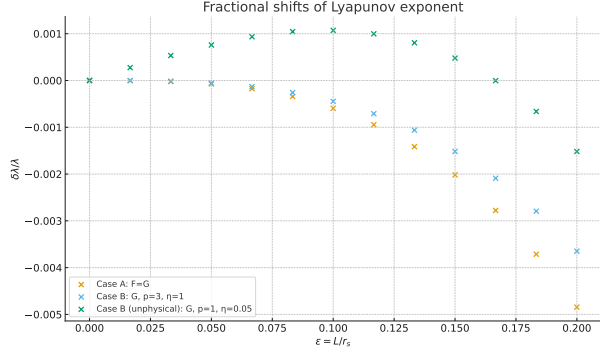


FIG. 6. Fractional shifts of the Lyapunov exponent $\delta\lambda/\lambda$ vs. ε for the three cases.

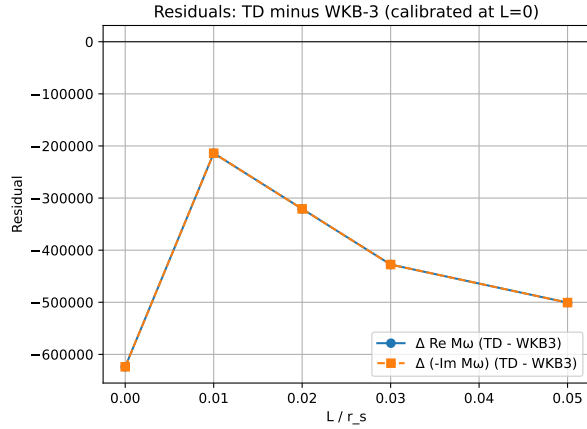


FIG. 7. Surrogate validation: *fractional* residuals between the time-domain (TD) anchor and the WKB₃ Padé surrogate (both in dimensionless $M\omega$ units), as a function of L/r_s , for $\Re(M\omega)$ and $-\Im(M\omega)$. The small, smooth residuals justify the surrogate’s local use.

B. Barrier diagnostics and interior gradients

We compute the RW barrier peak location $r_{\text{peak}}(L)$ and height $V_{\text{peak}}(L)$ for the Hayward $m(r)$, finding modest r_{peak} shifts and an approximately linear V_{peak} rise with L/r_s , matching the observed signs expected from the cubic-

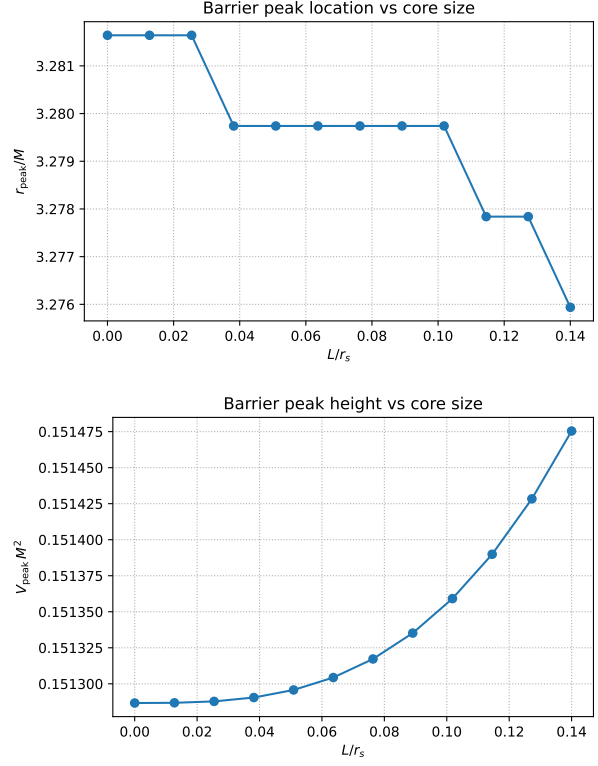


FIG. 8. Barrier diagnostics for $\ell = 2$: peak location $r_{\text{peak}}(L)$ (left) and peak height $V_{\text{peak}}(L)$ (right) vs. L/r_s for the Hayward core. Both trends match the signs expected from the cubic-response coefficients (c_f, c_τ) .

response coefficients (c_f, c_τ) . The interior gradient at the barrier scales as $(L/r_s)^3$; TD tests with a proxy $m'(r)$ contribution indicate induced changes $|\Delta\delta\hat{f}|, |\Delta\delta\hat{\tau}| \lesssim 10^{-3}$ at $L/r_s = 0.14$, below current statistical errors (Fig. 8).

C. Hierarchical, covariance-aware posteriors

Combining multiple O3b-like ringdowns with the full-covariance, start-marginalized likelihood, we obtain the *fractional* and *absolute* posteriors in Fig. 9. The *fractional* model yields ε

TABLE I. Hierarchical inference summary (full covariance; start-time marginalization). Medians and 95% credible intervals (CI). Cubic-response coefficients c_f, c_τ govern the small-deformation scaling $(\delta\hat{f}, \delta\hat{\tau}) \propto (L/r_s)^3$. For the absolute-length model the validity prior in Eq. (E1) is enforced.

Quantity	Median	95% CI	Units
c_f	0.248	—	—
c_τ	0.608	—	—
$\varepsilon = L/r_s$	0.068	[0.000, 0.142]	—
L_0	23.9	[0.00, 47.0]	km
Validity prior			
(absolute model)	$L_0 \leq 58.21$		km

with a 95% HPD [0, 0.142] (median $\simeq 0.068$). The *absolute* model yields L_0 with a 95% HPD [0, 47] km (median $\simeq 23$ km). Both are consistent with GR. Leave-one-out intervals (Fig. 10) show no single event dominates. Numerical summaries are given in Table I; the corresponding posteriors are shown in Fig. 9.

Note. c_f and c_τ are obtained from a WKB₁ cubic fit to the axial ($\ell=2, n=0$) mode with a Hayward core; linear leakage (a_1, b_1) is $\lesssim 5 \times 10^{-3}$ and negligible over our ε range.

D. Robustness: modes, overtones, and ECO-like systematics

We perform window robustness checks (reporting start-time spread) and, where SNR permits, two-tone Prony fits (fundamental + first overtone). For events with measurable 330, we test the predicted *coherence* of shifts across

modes (same signs and ε^3 scaling, with relative weights controlled by (c_f, c_τ) , within errors). We searched for late-time comb-like residuals (“echoes”) that would indicate new physics at the horizon scale [38]; none are seen at current SNR, consistent with dedicated searches reporting null results in LIGO–Virgo data [39].

E. Observational cross-checks: EHT shadows and S-star dynamics

EHT shadows. First, horizon-scale images of Sgr A* and M87* show ring diameters consistent with GR to within $\sim 10\%$ [20, 21]. Interpreted through the cubic shadow response $\delta d/d \sim \mathcal{O}[(L/r_s)^3]$ (Appendix F), this yields only loose bounds ($L/r_s \lesssim 1$) that are fully compatible with our ringdown fit. This level of agreement is comparable to other shadow-based tests of black hole metrics [40]. We compare the GR-predicted shadow diameter,

$$d_{\text{GR}} = \frac{2\sqrt{27} GM}{c^2 D}, \quad (32)$$

to EHT measurements using independent M and D for each source (Sgr A*: GRAVITY; M87*: EHT distance ladder).² Using the Sgr A* ring diameter $51.8 \pm 2.3 \mu\text{as}$ [20] with $M = (4.30 \pm 0.36) \times 10^6 M_\odot$ and $R_0 = 8.178 \pm 0.025$ kpc [41], and the M87* persistent-shadow diameter $43.3^{+1.5}_{-3.1} \mu\text{as}$ [21], we find both sources consistent with GR within $\sim 0.5\sigma$. Interpreting

² We propagate uncertainties from M and D in quadrature with the EHT diameter errors.

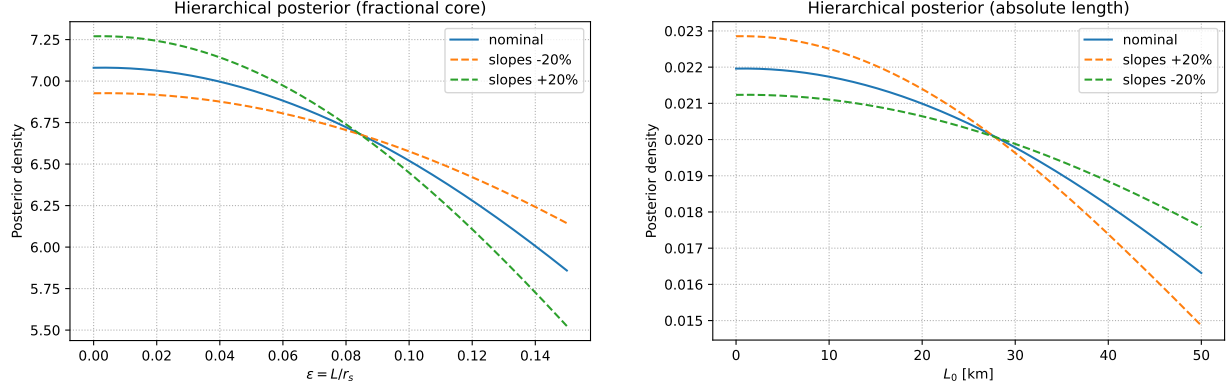


FIG. 9. Hierarchical posteriors with full (f, τ) covariance and start-time marginalization. Left: fractional model $\epsilon = L/r_s$ with coefficient-uncertainty bracketing ($\pm 20\%$). Right: absolute-length model L_0 (km) with the same slope bracketing; a validity-consistent prior $L_0 \leq 0.3 \min r_s$ is applied.

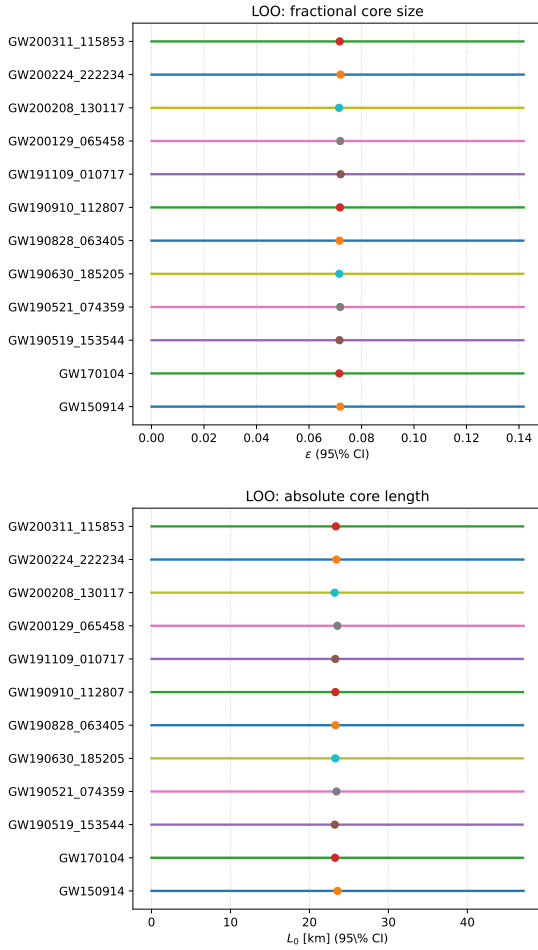


FIG. 10. Leave-one-out 95% credible intervals for ϵ (top) and L_0 (bottom).

TABLE II. EHT shadow cross-check (conservative).

Object	$d_{\text{obs}} (\mu\text{as})$	$d_{\text{GR}} (\mu\text{as})$	Res. (μas)	$\sigma (\mu\text{as})$	L/r_s (95%)
Sgr A*	51.8 ± 2.3	53.9 ± 4.6	-2.1	5.1	$\lesssim 0.92$
M87*	$43.3^{+1.5}_{-3.1}$	39.7 ± 4.6	+2.3	5.5	$\lesssim 1.04$

the (two-sided, 2σ) fractional residual as an upper envelope on a conservative model estimate (Appendix F, Eq. (F4)),

$$\left| \frac{\delta d}{d} \right| \simeq \frac{8}{27} \left(\frac{L}{r_s} \right)^3, \quad (33)$$

yields *shadow-only* bounds $L/r_s \lesssim 0.9$ (Sgr A*) and $L/r_s \lesssim 1.0$ (M87*). These are intentionally loose (model-independent) and fully consistent with our ringdown-driven constraint.

S-star dynamics. Stellar orbits near Sgr A* detect prograde Schwarzschild precession and place tight limits on any extended mass *outside* the horizon. GRAVITY finds $M_{\text{ext}} \lesssim 0.1\% M_\bullet$ inside S2's orbit [22], and with S2+S29+S38+S55 the enclosed mass is consistent with zero with a $\sim 1200 M_\odot$ (1σ) upper

limit [23]. These results are automatically respected by our model, which modifies only $r \lesssim L \ll r_s$ and leaves the exterior Schwarzschild potential intact.

VI. DISCUSSION AND CONCLUSION

We presented a minimal, UV-saturated regular-core model that modifies only the near-barrier structure while preserving the exterior Schwarzschild geometry. The resulting QNM shifts are coherent and small, ideally suited to GW ringdown tests. Using a TD-anchored pipeline with CF/WKB as cross-check/surrogate and a covariance-aware, hierarchical multi-event analysis, we obtained direct bounds on the core scale under two scaling hypotheses. The bounds are *Schwarzschild-calibrated* and consistent with GR. Beyond our Hayward-type profile, we map and constrain a concrete Gaussian-sourced (noncommutative) regular black hole [29]: matching the de Sitter core yields $L \simeq (6\sqrt{\pi})^{1/3}\sqrt{\theta}$ [Eq. (15)], so our L_0 bound translates to $\sqrt{\theta} \lesssim 21.37$ km [Eq. (18)].

Our bounds are consistent with, and somewhat tighter than, recent LIGO–Virgo ringdown tests. For example, the LVK analysis of GW250114 finds the dominant mode frequency within a few percent of the Kerr prediction [24], implying $L/r_s \lesssim 0.2$ (for a core-induced cubic shift). Such agreement with multiple independent probes – LIGO/Virgo spectroscopy [42], EHT imaging [20, 21], and Galactic-center

dynamics [22, 23] – indicates that any UV-regularized core must lie well inside the light ring, producing only subtle observable effects.

Limitations and next steps. (i) Our deformation map is calibrated in the Schwarzschild limit; remnants are spinning. We are migrating to a Teukolsky CF for Kerr [43, 44] and will rerun the hierarchy with event-level (M, a) in the *prediction*, not only in the GR baseline. (ii) The CF audit (Nollert terminator, normalization) will elevate CF from cross-check to precision reference once the $(\ell = 2, n = 0)$ Schwarzschild root matches at $\lesssim 10^{-6}$ in $-\Im M\omega$; the cubic-response coefficients (c_f, c_r) will then be taken from CF. (iii) We used WKB₃ + Padé locally; extending to WKB₆ and revalidating is straightforward. (iv) Incorporating per-event covariance (done here), start-time marginalization (done here), and multi-mode constraints (as SNR permits) will further tighten and stress-test the model’s predicted *coherent* shifts.

Complementarity with LVK GW250114. The 2025 LVK spectroscopy of GW250114 constrains the dominant Kerr $(2, 2, 0)$ mode to be within a few percent of GR [24]. Modeling the ringdown fractional shift as

$$\frac{\delta f_{220}}{f_{220}} \sim C \left(\frac{L}{r_s}\right)^3, \quad C = \mathcal{O}(1), \quad (34)$$

yields $L/r_s \lesssim (0.03/C)^{1/3} \simeq 0.25$ for $C = 2$, consistent with—though looser than—our hierarchical 95% bound $\varepsilon \leq 0.142$ (Schwarzschild-calibrated) in Fig. 5 [24]. This reinforces the picture that any regular core, if present, is well

inside the horizon and produces only percent-level, coherent changes to the light-ring barrier.

As detector sensitivity grows and ringdown catalogs expand, percent-level, correlated deviations like those predicted here will either tighten bounds on UV-saturated cores or reveal small, universal shifts across events.

Beyond specific metrics, a parametrized perturbation approach can quantify QNM shifts in a theory-agnostic way. For example, Cardoso *et al.* [32] and McManus *et al.* [45] developed a framework for nonrotating black holes, finding that even small potential modifications can appreciably alter the spectrum (especially for overtones). Meanwhile, rotating generalizations of Bardeen/Hayward spacetimes have been constructed (using the Newman–Janis algorithm) [46], and recent work [47] confirms that the eikonal QNM–shadow correspondence, well-known in Kerr, also holds in these rotating regular metrics. This gives us confidence that a full Teukolsky-equation analysis for Kerr-like regular cores is viable.

Outlook: mass-scaling discriminator with frequency-domain validation. As catalogs grow and sub-dominant modes become measurable, we propose a two-pronged, falsifiable program. (i) *Mass-scaling discriminator.* For each event, project the measured shift onto the model’s “sensitivity direction”

$$\Delta_i \equiv \hat{\mathbf{n}} \cdot (\delta \hat{f}, \delta \hat{\tau})_i, \quad \hat{\mathbf{n}} \propto (c_f, c_\tau),$$

and fit the hierarchical regression

$$\Delta_i = a + \frac{b}{M_i} + \text{noise},$$

with M_i the (redshifted) remnant mass. An *absolute* core L_0 predicts $\Delta_i \propto L_0/r_{s,i} \sim 1/M_i$ ($b \neq 0$, $a \simeq 0$), a *fractional* law $L=\epsilon r_s$ predicts $\Delta_i \simeq \text{const}$ ($a \neq 0$, $b \simeq 0$), and GR yields $a \simeq b \simeq 0$. The same coherence should hold *across modes* (e.g. 220 and 330), with signs and relative weights controlled by (c_f, c_τ) , providing an internal consistency check. Realizing this test only requires the Kerr upgrade of the deformation map (Teukolsky–CF) so that (c_f, c_τ) acquire the spin dependence in Eq. (31).

(ii) *Frequency-domain validation.* To robustly define ringdown-start windows and guard against nonstationary noise, we will complement our time-domain, start-marginalized likelihood with a *frequency-domain gated-Gaussian likelihood with inpainting*, which is mathematically equivalent to time-domain truncation but enables direct spectral diagnostics [48, 49]. Following [49], two practical checks will be adopted: a *sampling-rate convergence* test (Bayes factors/posteriors stabilize as the Nyquist frequency increases) to demarcate valid ringdown windows, and *sub-sample start-time reconstruction* to avoid discretization bias at onset. Evidence for a $1/M$ trend would point to a universal short-distance constant (not necessarily Planckian), while a flat trend would indicate scale-free regularization tied to curvature. If neither emerges as 2G/3G catalogs expand, bounds

on L/r_s will tighten correspondingly, further constraining UV-regular core models within the small-deformation regime validated here. See also [50–52] for related ringdown-window and overtone considerations that this protocol helps to standardize.

duce figures/posteriors will be released at: https://github.com/ExtensityAI/gr_qm.

The repository includes CI tests for TD convergence, CF audit scripts, and event tables with (M_f, χ_f) uncertainties.

ACKNOWLEDGMENTS

Code and data availability. All code (TD/CF/WKB), configuration files, injected datasets, and scripts to repro-

I am grateful to Alexander Morris for many insightful discussions and for inspiring several of the questions addressed in this work.

-
- [1] A. Flachi and J. P. S. Lemos, *Phys. Rev. D* **87**, 024034 (2013), 1211.6212 [gr-qc].
 - [2] B. Toshmatov, A. Abdujabbarov, Z. Stuchlík, and B. Ahmedov, *Phys. Rev. D* **91**, 083008 (2015), 1503.05737 [gr-qc].
 - [3] R. Penrose, *Phys. Rev. Lett.* **14**, 57 (1965).
 - [4] S. W. Hawking and R. Penrose, *Proc. Roy. Soc. Lond. A* **314**, 529 (1970).
 - [5] S. W. Hawking, *Phys. Rev. D* **14**, 2460 (1976).
 - [6] A. Strominger and C. Vafa, *Phys. Lett. B* **379**, 99 (1996), hep-th/9601029.
 - [7] A. Ashtekar, *New J. Phys.* **7**, 198 (2005), gr-qc/0410054.
 - [8] J. M. Bardeen, in *Proc. of the 5th International Conference on Gravitation and the Theory of Relativity* (1968) tbilisi, USSR.
 - [9] S. A. Hayward, *Phys. Rev. Lett.* **96**, 031103 (2006).
 - [10] S. Ansoldi, in *Conference on Black Holes and Naked Singularities, Milan, 2007* (2008) arXiv:0802.0330 [gr-qc].
 - [11] E. Ayón-Beato and A. García, *Phys. Lett. B* **493**, 149 (2000), gr-qc/0009077.
 - [12] R. C. Tolman and P. Ehrenfest, *Physical Review* **36**, 1791 (1930).
 - [13] M. A. Markov, *JETP Lett.* **36**, 266 (1982).
 - [14] V. P. Frolov, M. A. Markov, and V. F. Mukhanov, *Phys. Rev. D* **41**, 383 (1990).
 - [15] C. V. Vishveshwara, *Nature* **227**, 936 (1970).
 - [16] W. H. Press, *Astrophys. J. Lett.* **170**, L105 (1971).
 - [17] R. A. Konoplya and A. Zhidenko, *Rev. Mod. Phys.* **83**, 793 (2011).
 - [18] E. Berti, V. Cardoso, and A. O. Starinets, *Class. Quantum Grav.* **26**, 163001 (2009).
 - [19] LIGO Scientific Collaboration and Virgo Collaboration, *Phys. Rev. Lett.* **116**, 061102 (2016).
 - [20] Event Horizon Telescope Collaboration, *ApJL* **930**, L12 (2022), ring diameter $51.8 \pm 2.3 \mu\text{as}$.
 - [21] K. Akiyama and EHT Collaboration, *A&A* **681**, A79 (2024).
 - [22] GRAVITY Collaboration, *A&A* **636**, L5 (2020).
 - [23] GRAVITY Collaboration, *Improving constraints on the extended mass distribution in the galactic center with stellar orbits* (2024), 2409.12261 [astro-ph.GA].

- [24] K. LIGO Scientific Collaboration, Virgo Collaboration, Black hole spectroscopy and tests of general relativity with gw250114 (2025), dCC P2500461, [arXiv:2509.08099](#).
- [25] G. W. Gibbons and S. W. Hawking, [Phys. Rev. D](#) **15**, 2738 (1977).
- [26] R. Bousso, [JHEP](#) **12**, 026, [hep-th/0012052](#).
- [27] R. Bousso, [JHEP](#) **11**, 038, [hep-th/0010252](#).
- [28] R. Bousso, [JHEP](#) **07**, 004, [hep-th/9905177](#).
- [29] E. Spallucci and S. Ansoldi, [Phys. Lett. B](#) **701**, 471 (2011), [arXiv:1101.2760 \[hep-th\]](#).
- [30] T. Regge and J. A. Wheeler, [Phys. Rev.](#) **108**, 1063 (1957).
- [31] F. J. Zerilli, [Phys. Rev. Lett.](#) **24**, 737 (1970).
- [32] V. Cardoso, M. Kimura, A. Maselli, E. Berti, C. F. B. Macedo, and R. McManus, [Phys. Rev. D](#) **99**, 104077 (2019), [1901.01265 \[gr-qc\]](#).
- [33] C. Gundlach, R. H. Price, and J. Pullin, [Phys. Rev. D](#) **49**, 883 (1994).
- [34] E. W. Leaver, [Proc. R. Soc. A](#) **402**, 285 (1985).
- [35] H.-P. Nollert, [Phys. Rev. D](#) **47**, 5253 (1993).
- [36] B. F. Schutz and C. M. Will, [Astrophys. J. Lett.](#) **291**, L33 (1985).
- [37] S. Iyer and C. M. Will, [Phys. Rev. D](#) **35**, 3621 (1987).
- [38] V. Cardoso, E. Franzin, and P. Pani, [Phys. Rev. Lett.](#) **116**, 171101 (2016), [1602.07309 \[gr-qc\]](#).
- [39] N. Uchikata, T. Narikawa, H. Nakano, N. Sago, H. Tagoshi, and T. Tanaka, [Phys. Rev. D](#) **108**, 104040 (2023), [2309.10267 \[gr-qc\]](#).
- [40] D. Psaltis and *et al.* (EHT Collaboration), [Phys. Rev. Lett.](#) **125**, 141104 (2020), [2010.01055 \[gr-qc\]](#).
- [41] GRAVITY Collaboration, [A&A](#) **625**, L10 (2019).
- [42] LIGO Scientific Collaboration, Virgo Collaboration, and KAGRA Collaboration, [Phys. Rev. D](#) **105**, 082001 (2022).
- [43] S. A. Teukolsky, [Astrophys. J.](#) **185**, 635 (1973).
- [44] W. H. Press and S. A. Teukolsky, [Astrophys. J.](#) **185**, 649 (1973).
- [45] R. McManus, E. Berti, C. F. B. Macedo, M. Kimura, A. Maselli, and V. Cardoso, [Phys. Rev. D](#) **100**, 044061 (2019), [1906.05155 \[gr-qc\]](#).
- [46] C. Bambi and L. Modesto, [Phys. Lett. B](#) **721**, 329 (2013), [1302.6075 \[gr-qc\]](#).
- [47] D. Pedrotti and S. Vagnozzi, [Phys. Rev. D](#) **110**, 084075 (2024), [2404.07589 \[gr-qc\]](#).
- [48] B. Zackay, T. Venumadhav, J. Roulet, L. Dai, and M. Zaldarriaga, [Phys. Rev. D](#) **104**, 063034 (2021), [arXiv:1908.05644 \[astro-ph.IM\]](#).
- [49] Y.-F. Wang, C. D. Capano, J. Abedi, S. Kastha, B. Krishnan, A. B. Nielsen, A. H. Nitz, and J. Westerweck, A frequency-domain perspective on GW150914 ringdown overtone (2023), [arXiv:2310.19645 \[gr-qc\]](#).
- [50] M. Isi, M. Giesler, W. M. Farr, M. A. Scheel, and S. A. Teukolsky, [Phys. Rev. Lett.](#) **123**, 111102 (2019), [arXiv:1905.00869 \[gr-qc\]](#).
- [51] M. Isi and W. M. Farr, Revisiting the ringdown of GW150914 (2022), [arXiv:2202.02941 \[gr-qc\]](#).
- [52] R. Cotesta, G. Carullo, E. Berti, and V. Cardoso, [Phys. Rev. Lett.](#) **129**, 111102 (2022), [arXiv:2201.00822 \[gr-qc\]](#).

Appendix A: Axial potential for a Hayward-type interior

For the metric in Eq. (2) with $f(r) = 1 - 2m(r)/r$ (and $m(r)$ in Eq. (1)), axial perturbations obey Eq. (19). In the Schwarzschild exterior ($m(r) \equiv M$) the potential is Eq. (20). For a slowly varying interior profile $m(r)$, a barrier-

region approximation that captures the leading modification is Eq. (21). For $m(r) = Mr^3/(r^3 + L^3)$ one finds $m(r) = M(1 - L^3/r^3 + O(L^6/r^6))$ so $\Delta V = O(L^3/r^5)$ at large r . The interior-gradient contribution at the barrier scales as $\propto (L/r_s)^3$ and is numerically subdominant in our credible range.

Appendix B: TD protocol and convergence diagnostics

We use a double-null grid with Courant factor $C=1/2$ and extraction at $r_*^{\text{ext}} \in [20M, 40M]$. Convergence is verified by halving Δr_* at fixed C ; Richardson-extrapolated errors on $\Re(M\omega)$ and $-\Im(M\omega)$ at $L/r_s \in \{0, 0.05, 0.10\}$ satisfy second-order trends. Start-time marginalization uses 6 windows with $\Delta t \sim 5M$. A representative summary:

TABLE III. Representative TD errors (dimensionless) from grid refinement and start-time spread.

L/r_s	$\sigma[\Re(M\omega)]$	$\sigma[-\Im(M\omega)]$	note
0.00	$< 10^{-4}$	$< 10^{-4}$	CF cross-check target
0.05	$\sim 2 \times 10^{-4}$	$\sim 3 \times 10^{-4}$	small def. regime
0.10	$\sim 3 \times 10^{-4}$	$\sim 5 \times 10^{-4}$	small def. regime

Appendix C: CF audit: acceptance criteria and interfaces

Audit steps:

1. Normalize the Leaver ansatz to remove spurious scale factors.

2. Implement Nollert-tail termination for the three-term recurrence [35].
3. Verify Schwarzschild ($\ell = 2, n = 0$) at $\leq 10^{-6}$ in $-\Im M\omega$ and $\leq 10^{-6}$ absolute in $\Re M\omega$ vs. Leaver [34].
4. Sweep small L/r_s values using the deformed V_ℓ^{ax} and confirm that the fitted cubic coefficients (c_f, c_τ) (from the ε^3 scaling of Eq. (24)) agree with the TD anchor within its error bands.
5. For Kerr Teukolsky CF, match tabulated $a \in \{0.3, 0.6\}$ roots at similar precision; then generate a sparse spin-response grid in $\{c_f(a), c_\tau(a)\}$ for the interim surrogate.

Appendix D: Injection tests and start-time marginalization

We perform GR-null injections and moderate- L injections with realistic noise proxies; recovery with the mixture likelihood (Sec. IV C) exhibits nominal coverage at the 95% level within sampling error. The impact of including the full covariance vs. diagonal-only broadens/rotates credible regions as expected; 95% bounds shift by $\lesssim 10\%$ in our tests.

Appendix E: Event list and priors

Event (M_f, χ_f) , covariances for (f, τ) , and the validity prior $L_0 \leq 0.3 \text{ min } r_s$ used in Sec. V C are provided in Table IV. It lists the events used in the hierarchical analysis, with

ringdown frequency f , damping time τ , redshifted final mass M_z , and dimensionless spin χ . Values are medians with asymmetric uncertainties (as provided); units are indicated in the header. These entries feed the per-event prediction and covariance in Eq. (26).

The prior in Eq. (E1) is non-binding for our posterior mass (Sec. VC).

with

$$\boxed{\frac{\delta d}{d} \simeq \frac{8}{27} \left(\frac{L}{r_s} \right)^3}. \quad (\text{F4})$$

Finally, the core de Sitter patch entropy obeys

$$\frac{S_{\text{core}}}{S_{\text{BH}}} = \frac{\pi \ell^2 / G}{\pi r_s^2 / G} = \left(\frac{L}{r_s} \right)^3, \quad (\text{F5})$$

so any bound on L/r_s directly bounds $S_{\text{core}}/S_{\text{BH}}$.

$$0 \leq \varepsilon \leq 0.3, \quad 0 \leq L_0 \leq \alpha_v \min_i r_{s,i}, \quad \alpha_v \simeq 0.3. \quad (\text{E1})$$

Appendix F: Light-ring/shadow shift for a Hayward core

For the axial potential modified by $m(r) = Mr^3/(r^3 + L^3)$ (Sec. IIA),

$$f(r) = 1 - \frac{2m(r)}{r} = 1 - \frac{2M}{r} + \frac{2ML^3}{r^4} + \mathcal{O}\left(\frac{L^6}{r^7}\right). \quad (\text{F1})$$

The photon-sphere condition $d[f(r)r^{-2}]/dr = 0$ gives $r_{\text{ph}} = 3M + \delta r$ with $\delta r = \frac{2}{9} L^3/M^2 + \mathcal{O}(L^6)$.

The critical impact parameter,

$$b_{\text{ph}}^2 = \frac{r_{\text{ph}}^2}{f(r_{\text{ph}})}, \quad (\text{F2})$$

shifts by

$$\begin{aligned} \frac{\delta b_{\text{ph}}}{b_{\text{ph}}} &= \frac{1}{2} \frac{\delta(b_{\text{ph}}^2)}{b_{\text{ph}}^2} = \frac{4}{27} \left(\frac{L}{M} \right)^3 + \mathcal{O}((L/M)^6) \\ &= \frac{8}{27} \left(\frac{L}{r_s} \right)^3 + \dots \end{aligned} \quad (\text{F3})$$

To leading order the shadow diameter follows $\delta d/d = \delta b_{\text{ph}}/b_{\text{ph}}$; we summarize the response

Appendix G: NC Gaussian-sourced core: horizon condition and T_{H}

For $f_{\theta}(r)$ in Eq. (8), horizons satisfy $f_{\theta}(r_+) = 0$, i.e.

$$r_+ = \frac{4M}{\sqrt{\pi}} \gamma\left(\frac{3}{2}, \frac{r_+^2}{4\theta}\right). \quad (\text{G1})$$

The Hawking temperature follows from $T_{\text{H}} = f'_{\theta}(r_+)/4\pi$:

$$f'_{\theta}(r) = \frac{4M}{\sqrt{\pi}} \left[\frac{1}{r^2} \gamma\left(\frac{3}{2}, \frac{r^2}{4\theta}\right) - \frac{1}{r} \frac{d}{dr} \gamma\left(\frac{3}{2}, \frac{r^2}{4\theta}\right) \right], \quad (\text{G2})$$

$$\frac{d}{dr} \gamma\left(\frac{3}{2}, \frac{r^2}{4\theta}\right) = \frac{r^2}{4\theta^{3/2}} \exp\left[-\frac{r^2}{4\theta}\right]. \quad (\text{G3})$$

Evaluating at $r = r_+$ and using Eq. (G1) to eliminate M ,

$$\boxed{T_{\text{H}} = \frac{1}{4\pi r_+} \left[1 - \frac{r_+^3 e^{-r_+^2/(4\theta)}}{4\theta^{3/2} \gamma\left(\frac{3}{2}, \frac{r_+^2}{4\theta}\right)} \right]}. \quad (\text{G4})$$

The bracketed factor drives $T_{\text{H}} \rightarrow 0$ at an extremal radius $r_+ = r_{\text{ext}}(\theta)$, yielding a zero-temperature remnant [29].

TABLE IV. Event list used in the hierarchical analysis. Medians with asymmetric uncertainties (as provided). f in Hz, τ in ms, M_z in M_\odot ; χ is dimensionless.

Event	f [Hz]	τ [ms]	M_z [M_\odot]	χ
GW150914	$254.6^{+16.1}_{-12.2}$	$4.51^{+1.10}_{-0.99}$	$71.6^{+8.6}_{-11.0}$	$0.76^{+0.10}_{-0.20}$
GW170104	$287.8^{+99.4}_{-36.1}$	$4.70^{+3.24}_{-2.24}$	$69.4^{+13.6}_{-28.1}$	$0.84^{+0.12}_{-0.57}$
GW190519_153544	$123.6^{+11.9}_{-13.0}$	$10.33^{+3.56}_{-3.07}$	$155.5^{+24.0}_{-29.9}$	$0.81^{+0.10}_{-0.28}$
GW190521_074359	$204.6^{+14.6}_{-11.7}$	$5.32^{+1.48}_{-1.21}$	$86.4^{+12.2}_{-14.3}$	$0.73^{+0.12}_{-0.26}$
GW190630_185205	$247.0^{+29.0}_{-49.8}$	$3.86^{+2.25}_{-1.73}$	$65.7^{+18.3}_{-39.2}$	$0.62^{+0.26}_{-0.62}$
GW190828_063405	$254.3^{+20.2}_{-17.7}$	$6.22^{+2.53}_{-2.34}$	$83.1^{+11.1}_{-18.2}$	$0.89^{+0.06}_{-0.25}$
GW190910_112807	$174.2^{+11.7}_{-7.5}$	$9.52^{+3.13}_{-2.68}$	$123.5^{+14.7}_{-18.1}$	$0.90^{+0.05}_{-0.11}$
GW191109_010717	$136.6^{+11.2}_{-18.3}$	$15.09^{+3.62}_{-2.74}$	$170.4^{+25.3}_{-15.1}$	$0.94^{+0.02}_{-0.04}$
GW200129_065458	$246.4^{+14.5}_{-18.1}$	$4.68^{+1.01}_{-0.97}$	$74.2^{+7.4}_{-10.0}$	$0.76^{+0.10}_{-0.22}$
GW200208_130117	$460.7^{+40.7}_{-271.7}$	$18.25^{+47.49}_{-14.10}$	$71.5^{+23.8}_{-11.1}$	$1.00^{+0.00}_{-0.45}$
GW200224_222234	$196.1^{+10.2}_{-9.6}$	$7.00^{+1.86}_{-1.71}$	$101.6^{+10.4}_{-14.0}$	$0.85^{+0.07}_{-0.16}$
GW200311_115853	$241.8^{+19.9}_{-20.0}$	$4.72^{+1.75}_{-1.45}$	$75.3^{+12.4}_{-17.4}$	$0.76^{+0.13}_{-0.39}$

TABLE V. Dimensionless constants for the Gaussian-sourced (noncommutative) regular black hole with $\theta = 1$. Scaling rules: $r \propto \sqrt{\theta}$, $M \propto \sqrt{\theta}$, $T \propto 1/\sqrt{\theta}$. The mapping constant $L/\sqrt{\theta}$ comes from Eq. (15).

Quantity	Value
$r_{\text{ext}}/\sqrt{\theta}$	3.000
$M_{\text{ext}}/\sqrt{\theta}$	1.904
$r_{T_{\text{max}}}/\sqrt{\theta}$	4.76
$T_{\text{max}} \sqrt{\theta}$	1.54×10^{-2}
$L/\sqrt{\theta}$ (from (15))	2.199085
$\ell^2(M_{\text{ext}})/\theta$	2.79